PNAS RESEARCH ARTICLE | ENVIRONMENTAL SCIENCES

Boosted ammonium production by single cobalt atom catalysts with high Faradic efficiencies

Jiacheng Li[a], Miao Li[a,1], Ning An[a], Shuo Zhang[a], Qinan Song[a], Yilin Yang[a], Jing Li[a], and Xiang Liu[a]

Edited by Alexis Bell, University of California, Berkeley, CA; received December 29, 2021; accepted April 1, 2022

Efficient $n = O$ bond activation is crucial for the catalytic reduction of nitrogen compounds, which is highly affected by the construction of active centers. In this study, $n = O$ bond activation was achieved by a single-atom catalyst (SAC) with phosphorus anchored on a Co active center to form intermediate *N*-species for further hydrogenation and reduction. Unique phosphorus-doped discontinuous active sites exhibit better $n = O$ activation performance than conventional *N*-cooperated single-atom sites, with a high Faradic efficiency of 92.0% and a maximum ammonia yield rate of 433.3 μg $NH4 \cdot h^{-1} \cdot cm^{-2}$. This approach of constructing environmental sites through heteroatom modification significantly improves atom efficiency and will guide the design of future functional SACs with wide-ranging applications.

nitrate | single-atom catalyst | cobalt | charge transfer | electrochemistry

Significance

The electrochemical reduction of nitrate to ammonia is a mild and efficient technique to reduce nitrate pollution in water and meet the demand for ammonia. Urgency for improvements in the efficiency of this process has accelerated the development of electrode materials. Herein, a phosphorus-modified cobalt single-atom catalyst (Co-SAC) was prepared with high atom economy based on the anchoring effect of a defect-rich carbon basal plane. The local environment of the Co atom was optimized by P-modification with asymmetric charge distribution and electron redistribution. The Co-SAC exhibited a high efficiency for ammonia production and good cycle stability due to its unique tetracoordinated structure, rendering it promising for the practical treatment of wastewater.

In 2020, Grade IV national surface quality was exceeded at 86.4% of 10,171 water quality monitoring points in China (1, 2). However, widespread nitrate (NO_3^-) pollution in water resources continues to threaten environmental safety and human health, and there is considerable pressure to ensure a guaranteed supply of safe drinking water (3). In a different context, ammonia (NH_3) is widely used as a valuable raw material for agricultural production, industrial feedstocks, and energy storage. Ammonia is conventionally produced from N_2 and H_2 using the Haber–Bosch (H-B) process (4); however, owing to the high bond dissociation energy of N≡N (941 $kJ \cdot mol^{-1}$), the H-B process requires high temperatures (400 to 500 °C) and pressures (150 to 300 atm) (5), resulting in various safety considerations and high energy consumption. There is therefore a requirement for easy-to-operate, environmentally friendly, and economical NH_3 production routes. In this context, the direct reduction of aqueous nitrate to ammonia could mitigate nitrate pollution in water bodies as well as supplement ammonia production without exhausting fossil fuels. Indeed, the lower bond dissociation energy of $n = O$ (204 $kJ \cdot mol^{-1}$) renders NO_3^- waste an ideal nitrogen source for the synthesis of ammonia.

Electrochemical methods, which typically involve benign reaction conditions, easy operation, and high efficiencies, can directly reduce aqueous NO_3^- to NH_3. These processes require less energy than the H-B process and can address environmental issues by constructing a new nitrogen cycle between NO_3^- and NH_3. Conventional electrochemical methods for NO_3^- removal typically produce N_2, NH_3, N_2O, nitrite (NO_2^-), et al.; many catalysts, including metals and their oxides, alloys, polymers, and carbon materials, have been investigated for application in such electrochemical reactions (5–10). Recent studies have focused on optimizing the catalyst structure to achieve a higher NO_3^- conversion (11). For example, TiO_2 nanotubes containing numerous oxygen vacancies exhibited a high Faradic efficiency (85.0%) for NO_3^- electroreduction, which was attributed to the inhibition of side reactions and the weakening of N–O bonds by oxygen vacancies (8). In addition, a Co_3O_4–TiO_2/Ti cathode exhibited good NO_3^- removal performance (9), while P doping generated additional empty d orbitals and increased the Co^{3+} content, resulting in an 8.45-fold improvement in the NO_3^- reduction rate (12). A previous study indicates that the Co-based catalyst had a better catalytic performance in nitrate electroreduction than other common transition metals such as Fe and Ni (13). The density functional theory (DFT) calculation also indicates that the hydrogenation of the N* intermediate and the adsorption of NH3* have moderate activation energies (5). Thus, the selectivity to ammonia is high over the Co-based catalyst, and cobalt has advantages in nitrate reduction compared with other transition metals. However, the occurrence of side reactions still challenges product selectivity, and the nanometer-sized Co active metal centers present in the catalyst inevitably produce N_2 during the NO_3^- electroreduction process (13, 14).

To address various energy and environmental issues, single-atom catalysts (SACs) have been developed (15–17). Their unique electronic properties and high metal

Author affiliations: [a]School of Environment, Tsinghua University, Beijing 100084, China

Author contributions: Jiacheng Li and M.L. designed research; Jiacheng Li, M.L., N.A., S.Z., Q.S., Y.Y., Jing Li, and X.L. performed research; Jiacheng Li and M.L. contributed new reagents/analytic tools; Jiacheng Li and M.L. analyzed data; and Jiacheng Li and M.L. wrote the paper.

The authors declare no competing interest.

This article is a PNAS Direct Submission.

[1]To whom correspondence may be addressed. Email: miaoli@tsinghua.edu.cn.

This article contains supporting information online at http://www.pnas.org/lookup/suppl/doi:10.1073/pnas.2123450119/-/DCSupplemental.

Published July 12, 2022.

utilization provide superlative catalytic activity and stability in various electrochemical reactions (17). For example, *N*-containing carbon materials supporting single metal atoms with metal–N_4 coordination sites exhibit ideal catalytic performances owing to their high metal loadings, adjustable structures, and high surface areas (18). In addition, the presence of intrinsic carbon defects and heteroatom doping defects (19) can also offer anchoring sites for single metal atoms and thereby improve catalytic performances (18). More specifically, catalytic performances can be optimized by altering the electronegativity by introducing heteroatom dopants that replace an N atom in the metal–N_4 active center. For example, substituting N with the less electronegative element P reduces the adsorption energies of reaction intermediates at the metal centers, thereby accelerating the reaction kinetics (20, 21).

Herein, Co-SACs supported on an *N*-doped carbon basal plane were further modified with P to increase the number of defects and provide additional anchoring sites for single metal atoms with strong metal–support interactions (SMSIs) and CoP_1N_3 coordination structures. Both Co–N and Co–P bonds were formed in a CoP_1N_3 configuration, where Co is directly tetracoordinated with one P atom and three N atoms. As N_2 formation requires the presence of consecutive active sites, it is expected that Co-SACs will effectively inhibit the N–N coupling step, and so the discrete Co active sites will not only accelerate the activation of NO_3^- but will also improve selectivity toward NH_4^+. Thus, the catalytic performance of the Co-SACs in the electroreduction of NO_3^- was evaluated, and their Faradic efficiencies in the production of NH_4^+ were determined. When assisted with other ammonia recovery methods, the application of Co-SACs in nitrate electroreduction is expected to promote a sustainable *N*-cycle and ammonia utilization (Fig. 1). The coordination environment of the Co atom was constructed through N and P modification, which significantly improved the atomic efficiency. In addition, this study offers a strategy to improve the catalytic performance of SACs by P modification in other electrochemical reactions.

Results

Characterization of SACs. Fig. 2*A* illustrates the fabrication process for Co-SACs with defect-rich supports. Co-SACs supported on *N*-doped and P/N-codoped carbon basal planes (denoted Co-CN and Co-CNP, respectively) were prepared by solid-state grinding and high-temperature pyrolysis using pyromellitic dianhydride, urea, ammonium chloride, and cobalt chloride as precursors and phytic acid as the P source. Transmission electron microscopy (TEM) images (Fig. 2*B* and *SI Appendix*, Fig. S1) showed that neither Co-CNP nor Co-CN contained large cobalt nanoparticles, and the carbon support was an irregular sheet, as shown in the scanning electron microscopy image (*SI Appendix*, Fig. S2). The high-resolution TEM image (Fig. 2*C*) excluded the presence of small Co clusters and showed that the surface of the P/N-codoped carbon basal plane was not smooth but wrinkled with many folds and defects. This irregular surface could offer anchoring sites for the stable loading of single Co atoms.

Aberration-corrected high-angle annular dark-field scanning TEM (HAADF-STEM) images (Fig. 2 *D* and *E*) with sub-ångström resolution confirmed the atomic distribution of Co atoms. The number of basal carbon layers and the roughness of the basal surface were both different, which resulted in different spots brightness of cobalt atoms; some of them with high brightness were signed by the yellow circles. Energy-dispersive X-ray spectroscopy (EDS) and elemental mapping images (Fig. 2 *F* and *G*) of Co-CNP showed signals corresponding to C, N, P, and Co, confirming the successful introduction of P. The mapping results also revealed a uniform distribution of Co

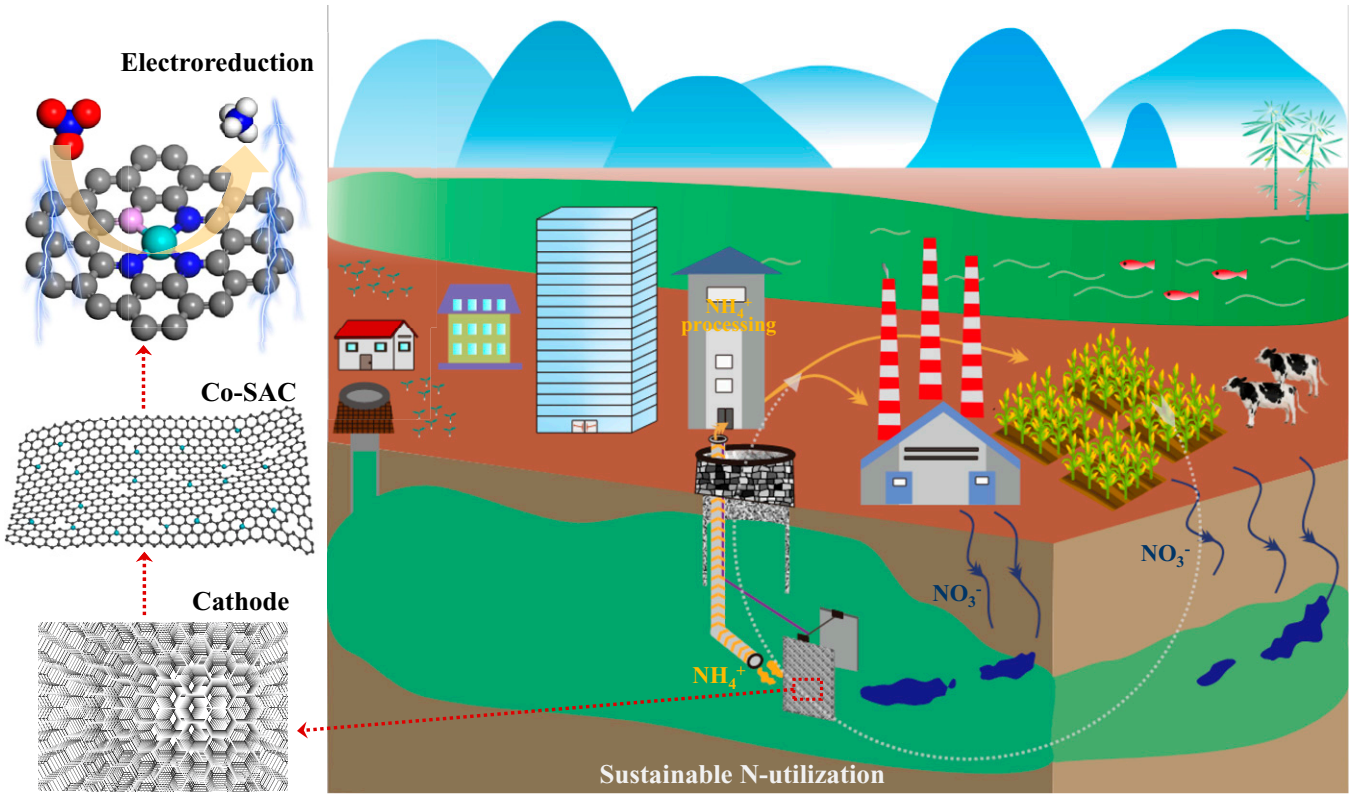

Fig. 1. Schematic drawing of sustainable *N*-utilization with the help of Co-SAC by electroreduction. The nitrate is first reduced on a Co-SAC by an electrochemical device, and the ammonia product is recovered for further utilization.

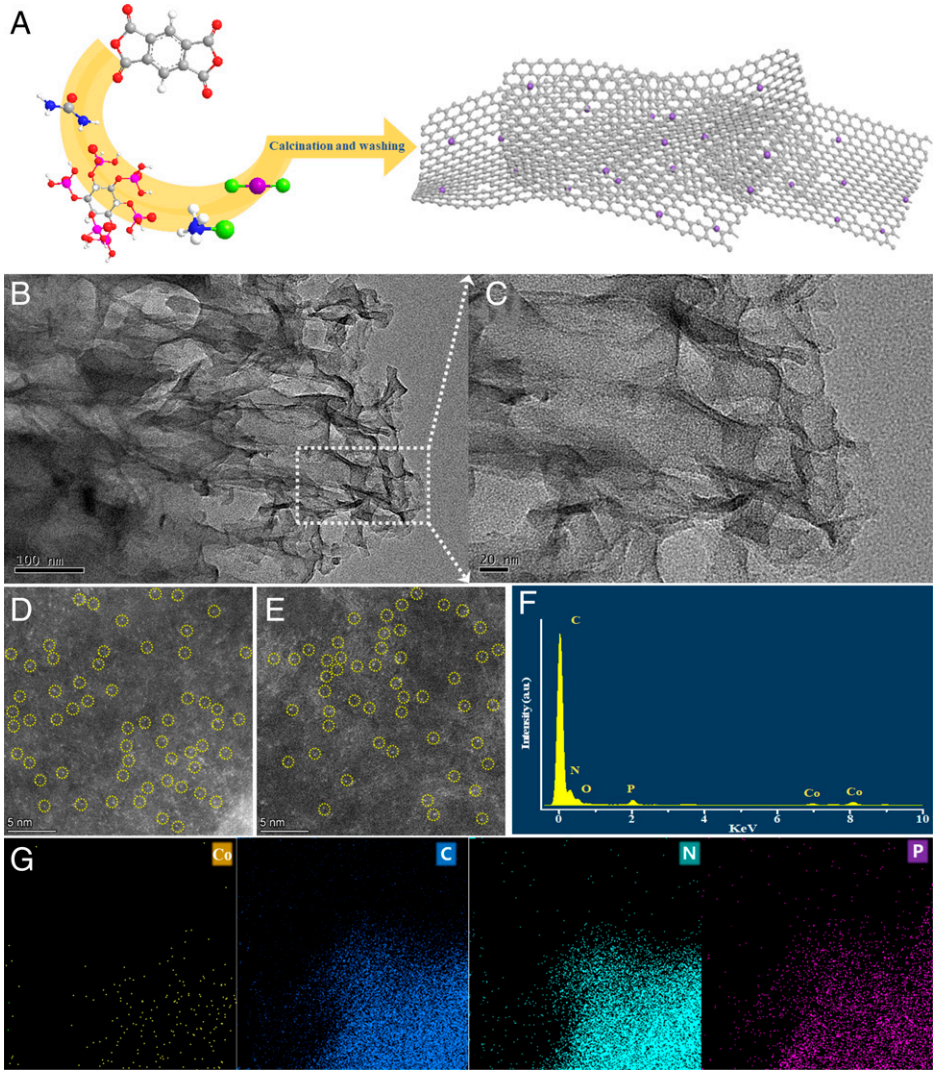

Fig. 2. Characterization of supports and SACs. (*A*) Illustration of the preparation of Co SACs. (*B and C*) TEM image (*B*) and high-resolution TEM image (*C*) of Co-CNP. (*D* and *E*) HAADF-STEM images of Co-CN (*D*) and Co-CNP (*E*); the bright spots marked with yellow circles represent single Co atoms. (*F*) EDS results for Co-CNP. (*G*) Elemental mapping images of Co (yellow), C (blue), N (green), and P (purple). a.u., arbitrary units.

atoms on the basal plane. Inductively coupled plasma optical emission spectrometry gave Co contents of 2.1 and 1.9 wt% for Co-CN and Co-CNP, respectively.

X-ray absorption spectroscopy (XAS), including both extended X-ray absorption fine structure (EXAFS) and X-ray absorption near-edge structure (XANES) analyses, has been widely used to reveal the electronic and geometric structures of SACs (21–23). Owing to its sensitivity to local structure, EXAFS fitting can provide the average coordination structure of metal centers (20, 22, 23).

To analyze the valence states, the XANES spectra of Co foil, Co_3O_4, CoP, Co-CN, and Co-CNP were collected at the Co K-edge (Fig. 3*A*). The Co K-edges of both Co-CNP and Co-CN were located between those of Co foil and Co_3O_4 in the red region. Thus, the Co center of each SAC had a higher valence than that of metallic Co^0 but was less positively charged than Co in Co_3O_4. The electrons of Co could be transferred to neighboring N or P atoms.

The k^2-weighted Fourier transform (FT)–EXAFS spectra were analyzed (Fig. 3*B*) to reveal the type of bonding between the Co atoms and their neighboring atoms. The EXAFS spectra of Co_3O_4 showed typical peaks at 2.20 and 1.48 Å corresponding to Co–Co and Co–O scattering, respectively. In contrast, Co-CN showed only one peak centered at 1.47 Å resulting from Co–N; the absence of a Co–Co peak indicates that Co was highly dispersed without forming nanoparticles or clusters. Thus, single-atom Co species were formed that interacted with N in the carbon basal plane in a CoN_4 configuration. Moreover, the X-ray diffraction (XRD) patterns of the Co-SACs (*SI Appendix*, Fig. S3) showed a broad peak corresponding to amorphous carbon without any pronounced peaks corresponding to Co nanocrystals, indicating no crystallized Co species on the support and confirming the high dispersion of Co.

In the FT-EXAFS spectrum of Co-CNP, a broad peak was observed at 1 to 2 Å, which could be fitted to two peaks ascribed to Co–N bonds and Co–P bonds at 1.75 Å. After P doping, one N atom in the CoN_4 configuration was replaced by a P atom and a P atom was directly coordinated with a Co atom. Quantitative fitting of the EXAFS data gave detailed coordination information about the Co active center. The obtained structural parameters, including coordination number, bond species, and interatomic distances, are summarized in *SI Appendix*, Table S1. The fitting results agreed with previously reported parameters for Co-SACs(20).

The wavelet transform (WT)–EXAFS spectra were analyzed with resolution in both radial space and k-space to confirm the

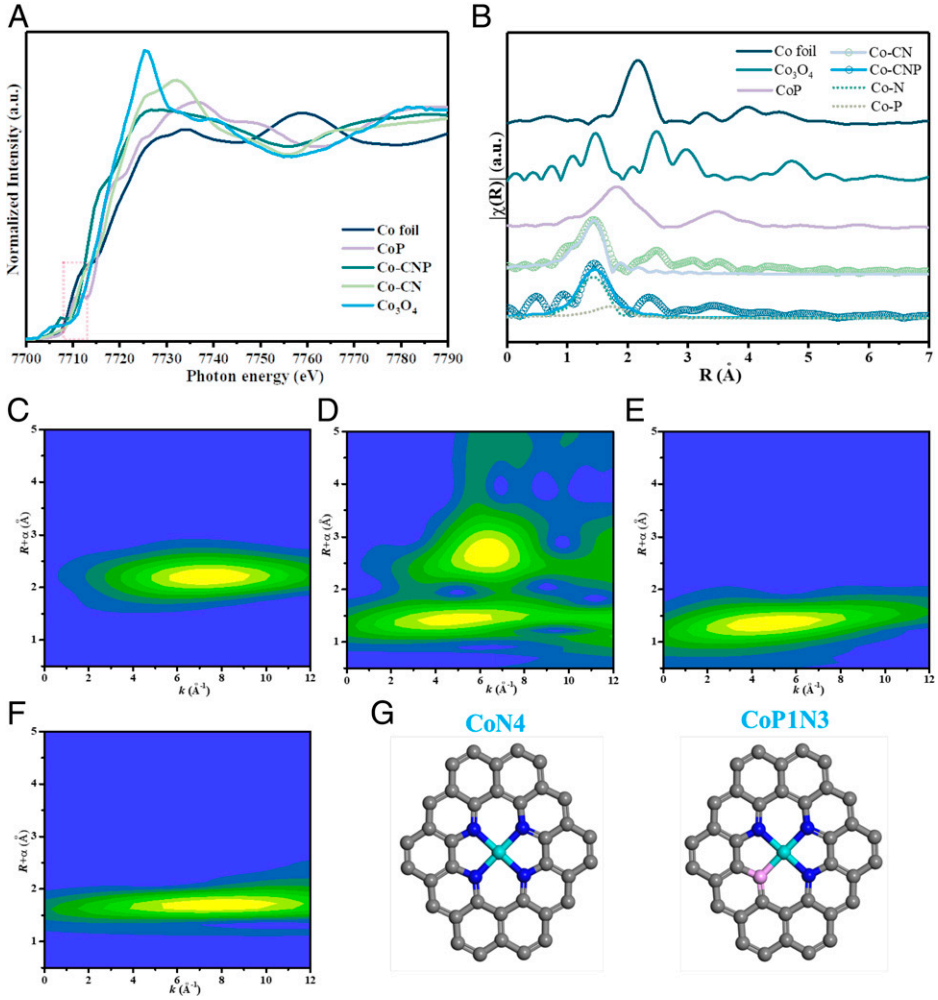

Fig. 3. Coordination environments of Co atom centers in SACs. (*A* and *B*) Normalized XANES spectra of Co foil, Co_3O_4, CoP, Co-CN, and Co-CNP at the Co K-edge (*A*) and corresponding k^2-weighted FT-EXAFS spectra (*B*). (*C*–*F*) WT-EXAFS contour plots of Co foil (*C*), Co_3O_4 (*D*), Co-CN (*E*), and Co-CNP (*F*). (*G*) Fitted configuration models for CoN_4 and CoP_1N_3 in Co-CN and Co-CNP. The gray, blue, pink, and cyan balls refer to C, N, P, and Co atoms, respectively. a.u., arbitrary units.

atomic dispersion and coordination states of Co. The WT-EXAFS spectra of Co foil and Co_3O_4 showed maxima at 6.7 and 6.2 $Å^{-1}$, which were ascribed to Co–Co and Co–O, respectively. In contrast, the WT contour plot of Co-CN showed a maximum centered at 4.4 $Å^{-1}$ corresponding to Co–N bonding (24). Similarly, Co-CNP displayed a maximum at 4.4 $Å^{-1}$ for Co–N, but maxima were also observed at 7.5 and 9.5 $Å^{-1}$, which were attributed to Co–P bonding (20). Consequently, the Co species were atomically dispersed, and CoN_4 and CoP_1N_3 models were built based on the FT- and WT-EXAFS results (Fig. 3*G*). This substitution of one N atom neighboring Co by P changed the local coordination structure and electron density of the Co active center.

The bonding structures of the elements neighboring the Co center were analyzed using soft XANES. The N K-edge XANES spectrum (Fig. 4*A*) showed three peaks associated with aromatic C–N–C bonds, graphitic N–3C bonds, and C–N σ bonds (25). The splitting of the first peak suggested Co–P bond formation (26).

High-resolution X-ray photoelectron spectroscopy (XPS) can supplement XAS results, providing chemical environment and bonding information for metal centers or surrounding light heteroatoms. The C 1s XPS profile of Co-CNP (*SI Appendix*, Fig. S4) showed peaks at 287.2, 285.9, and 284.9 eV corresponding to C–O, C–N, and C = C bonds (25, 27, 28), indicating successful N doping of the carbon basal plane. The broad peak in the N 1s XPS profile (Fig. 4*B*) was deconvoluted to give peaks at 398.6, 399.8, and 401.0 eV associated with pyridinic N, Co–N, and graphitic N, respectively (29). Co–N bond formation was also supported by the Co 2p XPS profile (*SI Appendix*, Fig. S4), which showed main peaks at 781.8 and 796.5 eV with corresponding satellite peaks at 783.8 and 798.0 eV in the Co $2p_{3/2}$ and Co $2p_{1/2}$ regions, respectively (30). As these peaks differed from those of metallic Co^0 nanoparticles (794.7 and 779.2 eV), they were ascribed to Co–N and Co–P bonds with positively charged single Co atoms. The corresponding Co 2p, C 1s, and N 1s XPS profiles of Co-CN are shown in *SI Appendix*, Fig. S5.

Successful P doping was confirmed by the P L-edge XANES spectrum of Co-CNP (Fig. 4*C*), which featured a peak at 142.4 eV attributable to C/N–P bonds (26, 31). Furthermore, the P 2p XPS profile (Fig. 4*D*) showed one main peak that was deconvoluted into two small peaks at 133.1 and 133.9 eV, ascribed to P–C and P–N bonds, respectively (20). The C K-edge XANES spectrum of Co-CNP (*SI Appendix*, Fig. S5*C*) exhibited a broad peak at 286.2 eV with a shoulder at 288.6 eV, corresponding to C = C rings and C–N or C–P bonds, respectively (20). Fourier transform infrared (FTIR) spectroscopy (*SI Appendix*, Fig. S6) verified the successful doping of P in Co-CNP, with two new bands observed at 750 and 1,450 cm^{-1}

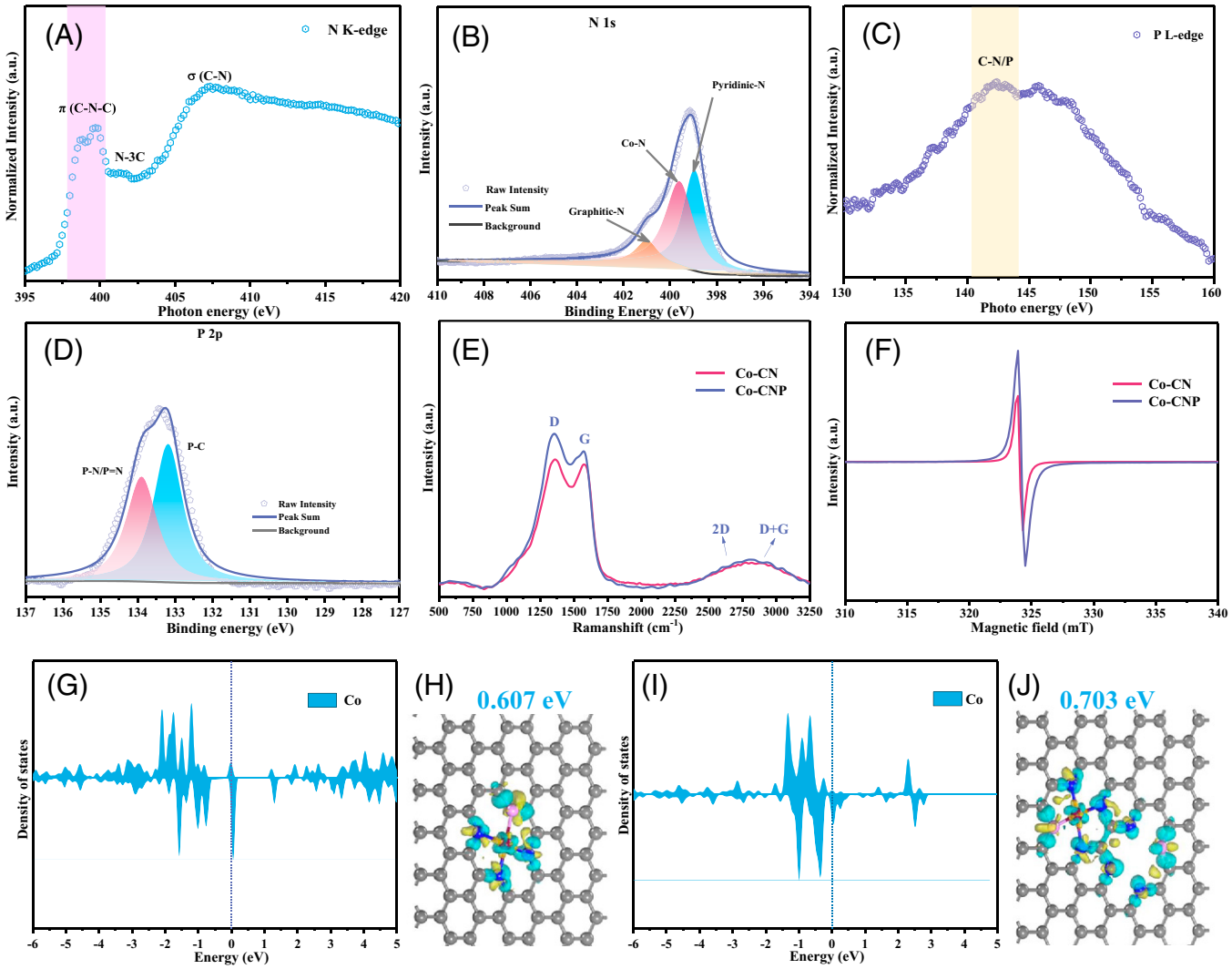

Fig. 4. Bonding information for light elements and electronic states of SAC active centers. (*A*) N K-edge soft XANES spectrum of Co-CNP. (*B*) Deconvoluted high-resolution N 1s XPS profile of Co-CNP. (*C*) P L-edge soft XANES spectrum of Co-CNP. (*D*) Deconvoluted high-resolution of P 2p XPS profile of Co-CNP. (*E*) Raman spectra of Co-CN and Co-CNP. (*F*) EPR spectra of Co-CN and Co-CNP. (*G* and *I*) PDOS for the CoP_1N_3 center (*G*) and its interaction with P_1N_3 defects (*I*). (*H* and *J*) Charge density differences in CoP_1N_3 sites (*H*) and the interaction between CoP_1N_3 sites and P_1N_3 defects (*J*). The gray, blue, pink, and red balls refer to C, N, P, and Co atoms, respectively. The yellow and cyan areas represent electron accumulation and depletion, respectively. a.u., arbitrary units.

corresponding to the stretching vibrations of P–N–C and P–C bonds, respectively (32, 33). Together with the Co K-edge XAS analysis, these results indicate that both P and N atoms were successfully introduced into the carbon basal plane by forming Co–N and Co–P bonds, resulting in Co metal centers with CoN_4 and CoP_1N_3 configurations.

P modification of the *N*-doped carbon skeleton created more defect sites, which significantly affected the properties of the Co SACs. The Raman spectra (Fig. 4*E*) of Co-CNP and Co-CN displayed peaks at 1,572 and 1,354 cm^{-1} corresponding to the G-band of sp^2-hybridized C atoms and the D-band of carbon defects (34). The intensity ratio of these bands (I_D/I_G) is widely used to characterize the defect level in graphitic structures (35, 36). The I_D/I_G value increased from 1.04 to 1.13 after P doping, confirming the increased defect level of Co-CNP. The overlap between 2D and D+G bands in the 2,500 to 3,000 cm^{-1} region also indicated that the SACs had highly defective structures.

Electron paramagnetic resonance (EPR) spectroscopy (Fig. 4*F*) at room temperature was used to study the electronic structures and defect degree of the SACs. The signal intensity of Co-CNP was 1.7 times higher than that of Co-CN, which suggests that P doping resulted in more defects. Co-CNP also showed a strong absorption peak in the visible–near-infrared region of the ultraviolet-visible (UV–Vis) absorption spectrum (*SI Appendix*, Fig. S7), indicating that the N/P-codoped carbon basal planes have many π-electrons and interact with each other through π–π stacking (37). Thus, although the number of defect sites could not be confirmed, P doping clearly increased the defect degree in Co SACs. The incorporation of heteroatoms could change the ideal structure and cause defects within the sp^2 hybridized carbon network due to the different atomic sizes of carbon and heteroatom; both N and P were doped into the crystal lattice of graphite carbon with more defects. The defect sites in the N/P-codoped support provided vacancies for anchoring Co atoms and also promoted charge transfer owing to the uneven distribution of electrons at the defect sites. Unlike the CoN_4 configuration (38), the Co center in the CoP_1N_3 configuration was stabilized by both P and N atoms, resulting in a more asymmetric electron distribution owing to the different electronegativities of N and P. The charge-varied defect sites promoted electron transfer and reduced electric resistance; they may also offer anchoring sites for single metal atoms and thereby could improve the catalytic performance of

the SACs. As confirmed by the XANES and XPS analyses, the Co site in the CoP_1N_3 coordination center was positively charged because of the electron-withdrawing effect of neighboring pyridinic N and P.

Because an accurate defect structure was difficult to determine, CoP_1N_3 sites with Co vacancies were used as model P defects, and their effects on neighboring Co sites were investigated using DFT calculations. In addition to the ideal CoP_1N_3 configuration, a model combining P defects and CoP_1N_3 sites was simulated. Based on the charge density difference analysis (Fig. 4 *H* and *J*), the Co site charge increased from 0.607 eV in the ideal CoP_1N_3 structure to 0.703 eV in the CoP_1N_3 structure affected by neighboring defect sites, leading to a more asymmetric charge distribution. The local coordination environment of the Co atom was changed by P-modification with asymmetric charge distribution and electron redistribution. When defect effects were considered, the projected density of states (PDOS) of the Co center (Fig. 4 *G* and *I*) showed that charge transfer occurred from the third orbital near the Fermi level. Thus, the increase in defect sites resulting from P doping altered the local environment and electronic structure of the Co center owing to an SMSI effect. This effect could enhance the dispersion and stability of single Co atoms, thus improving NH_4^+-production performance.

Catalytic Activity. Electrochemical NO_3^- reduction reactions were conducted on the Co SACs to examine the NH_4^+-Faradic efficiency (NFE) and NH_4^+-yield rate (NYR). NH_4^+ production was monitored using UV–Vis spectrophotometry (Fig. 5*A*), and Co-CNP showed higher NFEs and NYRs than Co-CN at all potentials (Fig. 5*A*), indicating that P doping enhanced NO_3^- reduction. P doping increased the Brunauer–Emmett–Teller (BET) surface area and pore volume (*SI Appendix*, Fig. S8 and Table S2), creating more defect sites on the support. The superior activity of Co-CNP was attributed to the P-induced defect sites and the unique CoP_1N_3 configuration. The new defect sites changed the electron distribution in the support, resulting in better electrical conductivity. The Co coordination environment was also affected, and the electronic structure of the metal center was modulated by less electronegative P.

The NFE plot for Co-CNP exhibited a volcano curve with a maximum of 92.0% at −0.69 V (versus reverse hydrogen electrode [RHE]), which is among the highest for previously reported catalysts (*SI Appendix*, Table S3). Both SACs showed lower NFEs at potentials more negative than −0.69 V, likely due to competition from the hydrogen revolution reaction, as indicated by bubble formation on the cathode at lower potentials, which consumes more electricity and reduces NFE value. The NYR continually increased as a function of potential, as more electrons and atomic H* were produced at more negative potentials (4), which was beneficial for NO_3^- reduction and hydrogenation, and both SACs exhibited maximum NYRs of 433.3 $\mu g\ NH_4 \cdot h^{-1} \cdot cm^{-2}$.

Electrochemical experiments were performed using $^{15}NO_3^-$ as the N source for NH_3 production, as monitored by ^1H NMR spectroscopy (4, 8). The ^1H NMR spectra with $^{14}NO_3^-$ and $^{15}NO_3^-$ as reactants showed typical triple and double peaks (Fig. 5*B*) corresponding to the $^{14}NH_4^+$ and $^{15}NH_4^+$ products, respectively. For $^{15}NO_3^-$ electroreduction on Co-CN and Co-CNP, $^{15}NH_4^+$ production was quantified using the integrated peak area ratio of $^{15}NH_4^+/C_4H_4O_4$ (maleic acid, external standard) as a function of $^{15}NH_4^+$ concentration (*SI Appendix*, Fig. S9). The NFE determined by ^1H-NMR spectroscopy was 91.0% on Co-CNP at −0.69 V (Fig. 5*C*), which was superior to that for Co-CN, in good agreement with the UV–Vis spectrophotometry results (Fig. 5*A*). No NH_3 was detected when a pure Na_2SO_4 solution was used, which confirmed that NH_4^+ was solely generated by NO_3^- electroreduction.

Further electrochemical measurements were performed to investigate the electrochemical behavior of the Co SACs and the influence of P doping. Steady-state polarization was used to analyze the basic properties of the cathodes. NO_3^- electroreduction kinetics were analyzed using Tafel plots (Fig. 5*D*), which had slopes of 333 and 286 $mV \cdot decade^{-1}$ for Co-CN and Co-CNP, respectively. The lower Tafel slope of Co-CNP indicates that P doping reduced the overpotential for NO_3^- reduction, with faster NO_3^- reaction kinetics resulting from enhanced conductivity and electron transfer. The electrochemically active surface area (ECSA) was determined from the non-Faradic region of cyclic voltammetry (CV) measurements at different scan rates (*SI Appendix*, Fig. S10 and Table S2). The ECSA of Co-CNP (0.79 cm^2) was larger than that of Co-CN (0.49 cm^2), confirming the better catalytic performance of Co-CNP for NO_3^- electroreduction.

Linear sweep voltammetry (LSV) measurements were performed in NO_3^- solution. At high scan rates, the LSV curves of Co-CNP (Fig. 5*E*) showed a marked peak due to NO_3^- reduction at −0.5 V, whereas this peak was not observed in the LSV curves of Co-CN (*SI Appendix*, Fig. S11), indicating the enhanced NO_3^- reduction activity of Co-CNP. The current density of Co-CNP exceeded that of Co-CN in the entire potential window. The slope of the plot of peak current as a function of the square root of the scan rate gave a charge transfer number of ∼8, confirming that NO_3^- reduction to NH_4^+ was an $8e^-$ process. The reduction peak is believed to be caused by NO_3^- diffusion control (39). However, as the LSV curves of Co-CNP showed a reduction peak at −0.3 V in NO_2^- solution (*SI Appendix*, Fig. S11), NO_2^- diffusion control could also result in a reduction peak. Because NO_3^- is first reduced to NO_2^- and then continuously reduced to NH_4^+ and there was no NO_2^- reduction peak in the LSV curves of Co-CNP in NO_3^- solution, the electroreduction of the NO_2^- intermediate is believed to be controlled by the chemical reaction in the NO_3^- solution.

Transient-state electrochemical impedance spectroscopy (EIS) was used to analyze the resistance properties of the cathodes (Fig. 5*F*). The Nyquist plots of Co-CNP and Co-CN showed semicircles with different radii in the high-frequency region, indicating differences in their charge-transfer resistances (R_{ct}) (40). The lower R_{ct} of Co-CNP was attributed to its higher conductivity and lower electron transfer resistance. The steady-state and transient-state electrochemical analyses confirmed that the electronic structures of Co SACs were efficiently optimized by P doping. This modulation of the Co coordination environment affected intrinsic electrochemical behavior, thus promoting the catalytic performance and improving NFE value.

The reusability of Co-CNP for NO_3^- electroreduction was further examined by evaluating both the FE loss and the NH_4^+ yield (*SI Appendix*, Fig. S12), and there were only small NFE and NH_4^+ yield losses after five cycles. The NFE and NYR were kept above 90% and 410 $\mu g\ NH_4 \cdot h^{-1} \cdot cm^{-2}$ in the cycle tests, respectively. CV stability tests (*SI Appendix*, Fig. S13) showed almost no change in current density after 1,000 cycles. The Co-CNP showed both better NFE performance and long-term stability. The stability of tetracoordinated Co sites with Co–P and Co–N bonds was beneficial for NO_3^- electroreduction to NH_3. Thus, Co-CNP has high activity and a long operation life, making it a good candidate for practical electrochemical applications.

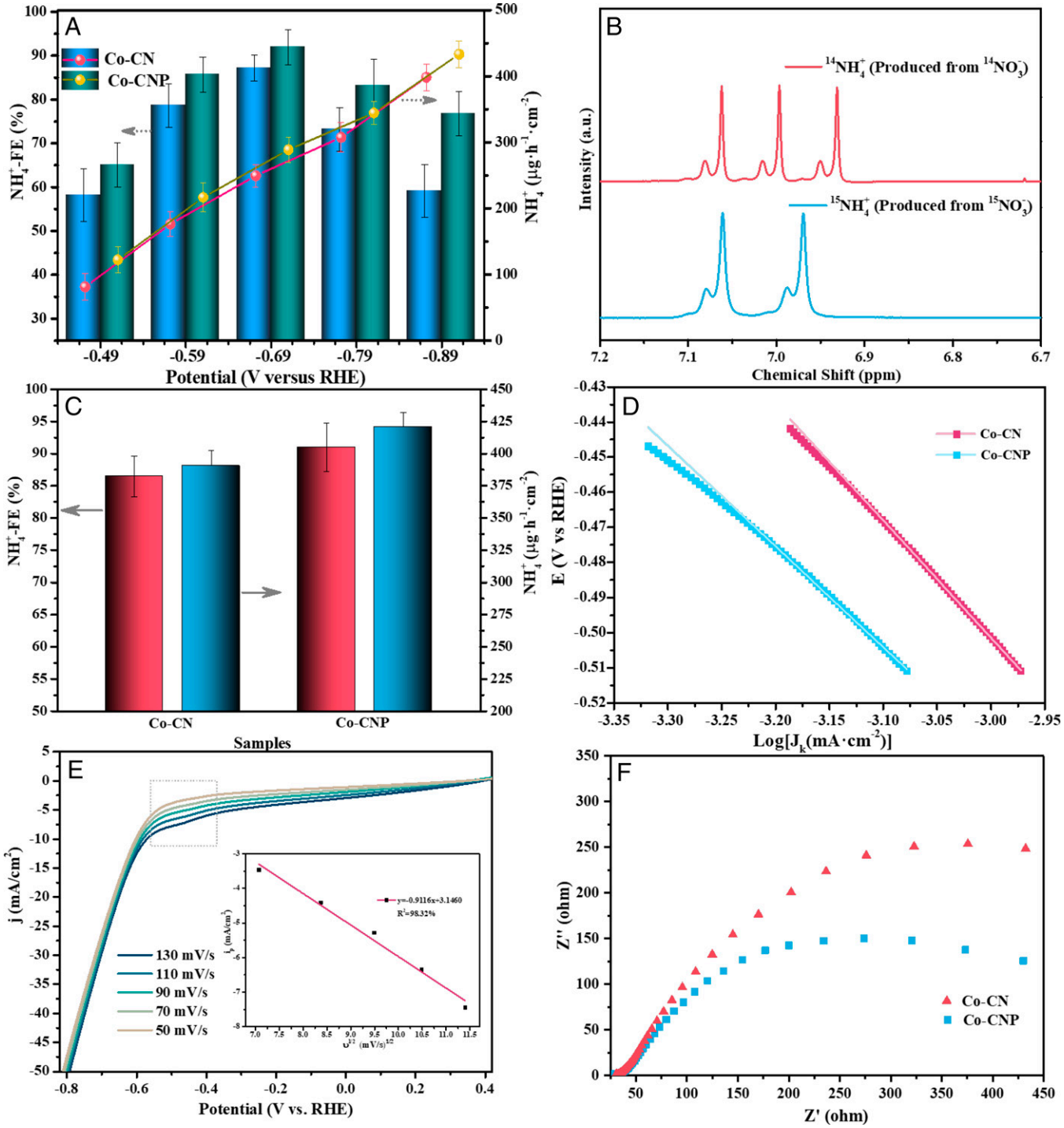

Fig. 5. Electrochemical performance of SACs. (*A*) NH_4^+-Faradic efficiency and NH_4^+-yield rate over Co-CN and Co-CNP at different potentials. (*B*) ^1H NMR spectra for NH_4^+ production after electroreduction. (*C*) NFEs and NYRs over Co-CN and Co-CNP at −0.69 V versus RHE. (*D*) Tafel slope analysis for Co-CN and Co-CNP. (*E*) LSV curves for Co-CN and Co-CNP (*Inset*: reduction peak current density as a function of the square root of the scan rate). (*F*) Nyquist plots for Co-CN and Co-CNP. a.u., arbitrary units.

Theoretical Analysis. NO_3^- electroreduction to NH_3 comprises several elementary reaction steps involving different intermediates and $8e^-$ transfer processes. Different reaction paths have been proposed in previous studies (14, 41, 42) because various electrocatalysts have been used and the reaction intermediates are complex. Generally, NO_3^- is first reduced to NO_2^-(43, 44) and then continually reduced to atomic N species that participate in N–N coupling or hydrogenation reactions, which determine the final N_2 or NH_4^+ selectivity (45).

To understand the reaction mechanism at the molecular level, the relationship between the structure and catalytic performance of Co SACs was analyzed using DFT calculations. NO_3^- reduction performance was examined via the *N*-end pathway, which also agreed with the pathways proposed by a previous study (13). Free energy change can predict the direction and feasibility of elementary steps according to thermodynamics. Free energy diagrams of each elementary reaction during NO_3^- reduction were analyzed using different active center models (Fig. 6 and *SI Appendix*, Figs. S14 and S15). NO_3^- was first adsorbed onto a

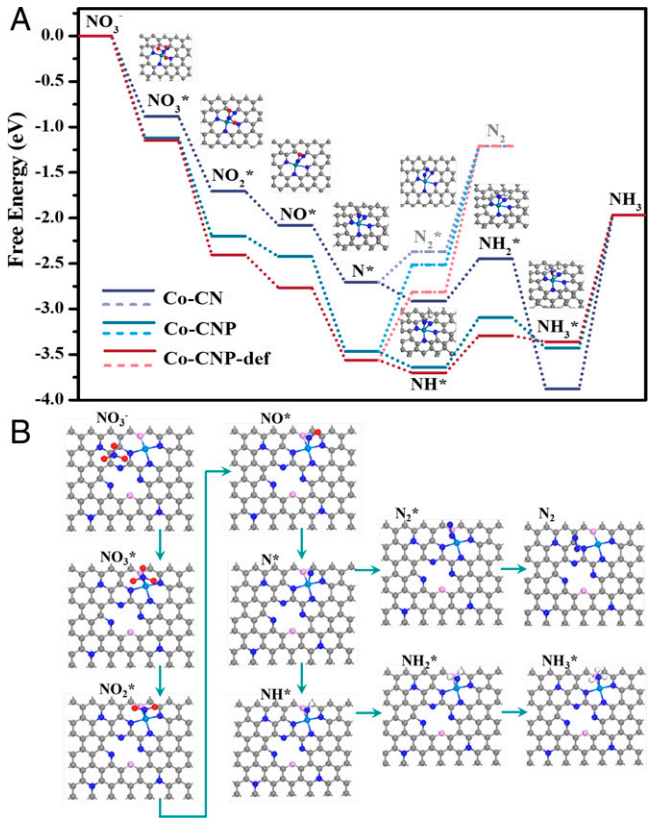

Fig. 6. DFT calculations for the NO_3^- electroreduction process. (*A*) Free energy changes for the elementary NO_3^- reduction steps on different SACs and adsorption models for different intermediates on the CoN_4 site. (*B*) Adsorption models on the CoP_1N_3 site affected by neighboring defect sites (The grey, blue, pink and cyan balls refer to C, N, P, and Co atoms, respectively.).

single Co site by the *N*-end configuration, where one O atom was lost to form NO_2*. The NO_3^{-}* to N* deoxygenation process was spontaneous and did not require extra energy. The energy changes for NO_3^- adsorption on Co-CN and Co-CNP were very different (0.88 and 1.11 eV, respectively). A larger adsorption energy change is beneficial for the formation of adsorbed NO_3^- and would facilitate NO_3^{-}* reduction in a diffusion-controlled reaction, in agreement with the higher NFE of Co-CNP. Notably, the hydrogenation of N* to NH* was downhill in free energy, whereas the N–N coupling reaction was uphill. As further hydrogenation was thermodynamically favored, N* was likely to combine with H* to form NH_4^+. As shown in *SI Appendix*, Fig. S15, all intermediate models were kept stable with *N*-end configuration in each elementary step. These DFT findings are in accordance with the experimental results, suggesting that the SACs exhibited enhanced NH_4^+ production owing to their discontinuous active metal sites. Such molecular-level insights into the catalytic performance of SACs with or without P modification could promote the design of SACs with higher NFEs and provide enhanced understanding of the reaction mechanism.

P doping formed numerous defects and resulted in the coordination of P atoms to Co centers, which affected the catalytic performance of Co SACs. Inspired by the charge density difference results, the intrinsic effect of P-induced defects on the activity of neighboring CoP_1N_3 sites was investigated by analyzing the free energy changes for the elementary reaction using DFT calculations. The energy diagrams for NO_3^- reduction on defect-neighboring Co sites showed the highest NO_3^- adsorption energy change (1.15 eV), and the protonation of *N to form *NH was also spontaneous. In contrast, on ideal CoP_1N_3, an extra energy barrier needed to be overcome, which indicates the promotion effect of P-induced defects on NH_4^+ production and the NFE. P doping could modulate the electronic density of Co sites at the atomic level and enhance NO_3^- electroreduction performance.

Conclusions

In summary, phosphorus-modified Co SACs were prepared by solid-phase grinding using a defect trapping strategy. The homogeneous distribution of Co atoms and their coordination configurations were identified by distinct HAADF-STEM images and XAS fitting analysis. Successful P doping was confirmed by XPS, soft XANES, and FTIR characterizations, which substituted the coordination element of N bonded with Co and created many defect sites on the C-*N* base as confirmed by EPR and Raman results. Therefore, the coordination environments of Co and the charge distribution of the support were modulated by P doping, which could further reduce nitrates and improve the NFE. Electrochemical reduction experiments showed that the Co-CNP SACs outperformed Co-CN SACs in the NFE and NYR, and P-modification effectively reduced the R_{ct} and overpotential. There is an SMSI effect between the Co atom center and defect-rich support as confirmed by the theoretical charge density difference analysis and experimental investigation, which not only improved NFE value but also promoted the stabilizations of Co atoms with good cycle activity. The produced ammonia could be recovered by different adsorbents through the ion exchange method (46–49), and the recovery could be continuously operated with the help of the electrochemically regenerated ion exchange method (50). The best operational conditions for ammonia production by nitrates could be identified and realized in practical wastewater treatment. In addition to developing efficient SACs with good prospects for practical applications, this work provides molecular-level insights into the reaction mechanism from the perspective of the SMSI effect, which could provide guidelines for designing high-efficiency SACs for various electrochemical reactions.

Methods

Preparation of SACs. The Co-CNP SAC was prepared using a solid phase grinding method (51) with some new modifications. Typically, solid powder of urea (4.2 g), ammonium chloride (1 g), pyromellitic dianhydride (2.2 g), phytic acid (0.12g), and cobalt chloride hexahydrate (0.26 g) were thoroughly mixed and continuously ground in an agate mortar. The mixture was then heated at 220 °C for 3 h and consequently washed by water, acetone, and ethanol three times. After drying in a vacuum oven, the mixture was further calcined for 3 h in a tube furnace and calcined at 500 °C with the heating rate of 2 °C min^{-1} under inert argon gas. The obtained sample was further treated with 0.5 M H_2SO_4 solution at 80 °C and washed with deionized water to get the final Co-CNP SACs. Similarly, Co-CN SACs were prepared without the P-precursor of phytic acid.

Characterization. A JEM-2010 electron microscope (JEOL) was used to obtain TEM images of SACs in large dimension. The high-resolution atomic images of different Co SACs were achieved in a Titan Cubed Themis G2 300 TEM apparatus (FEI) in the HAADF-STEM mode.

The Co K-edge XANES and EXAFS spectroscopy of different standard samples (Co foil, Co_3O_4, and CoP) and Co-SACs were recorded at room temperature using the 12-BM station of the Argonne National Laboratory in fluorescence mode. The energy was first calibrated by using Co foils as the standard reference sample. The C K-edge, N K-edge, and P L-edge soft XANES spectra of the Co-CNP were collected at the BL12B beamline of the National Synchrotron Radiation Laboratory (China). IFEFFIT software (implemented with Athena and Artemis modules)

was used to analyze and fit the acquired EXAFS data, obtaining the parameters to identify the configuration properties.

Inductively coupled plasma-optical emission spectrometry was used to quantitatively confirm the Co contents on an iCAP 7000 analyzer. The valence information of the composition elements in SACs was analyzed by XPS using a Thermo Fisher Scientific Escalab 250Xi–type photoelectron spectrometer. The XPS peak position was calibrated by the standard C 1s peak. A Nicolet iZ10 infrared spectrometer (Thermo Fisher Scientific) was used to record the FTIR spectra of the samples in the 400- to 4,000-cm^{-1} wavenumber, and the samples were mixed with KBr before testing. A D/max-IIIB diffractometer with Cu-Kα1 radiation (RIGAKU) was used to confirm the crystallinity of the SACs' powder, and the XRD patterns were obtained in the 2Θ range of 5 to 90°. Raman spectra were collected in a LabRAM HR Evolution spectrometer (HORIBA) using the 532-nm He–Ne radiation source. Each sample was tested for 20 s with three replications. A UV2700 spectrophotometer (Shimadzu) was used to get the UV–Vis absorption spectra of samples in the 200- to 800-nm wavelength range, where $BaSO_4$ is used as the standard reflectance. EPR spectroscopy was recorded at room temperature using a JEOL FA-200 instrument. N_2 adsorption–desorption isotherms were obtained in a Quantachrome Autosorb-1MP–type sorption analyzer. Both the BET and Barett–Joyner–Halenda methods were used to calculate the textural properties of samples such as specific surface area, pore size distribution, and pore volume.

Electrochemical Measurements. The working cathode was prepared by dropwise coating 140.6 μL catalyst ink on 2.25 cm^2 of nickel foam. The foam was dried in Ar and pressed under 10 Mpa of pressure to get the cathode plate. In detail, the catalyst ink was mixed with the Co-SAC powders, acetylene black, and polyvinylidene fluoride with the weight ratio of 8:1:1 in *N*-methyl-2-pyrrolidone solution. The solution was subsequently stirred and ultrasonicated to maintain uniformity before coating.

Nitrate electrochemical reduction was performed in a three-electrode electrolysis cell. Typically, 50 mL of electrolyte solution with 100 mg/L *N*-NO_3^- and 0.02 M Na_2SO_4 was used for the electroreduction test. The anode electrode and reference electrode were a commercial Ru-Ir-TiO_2 electrode and KCl-saturated Ag/AgCl electrode, respectively. The electrochemical measurements for NO_3^- reduction were conducted in a CHI-660E–type electrochemical workstation with the inner modular chronoamperometric (i–t) procedure. The recorded time curve for working potential and current density should remain stable before starting the electrochemical measurements. The potential of the Ag/AgCl electrode was calibrated to standard RHE based on the following equation:

$$E(RHE) = E(Ag/AgCl) + 0.22\ V + (0.059 \times pH) \quad [1]$$

The ammonia concentrations after reaction were quantitatively determined by colorimetric methods in a HACH DR UV spectrophotometer, and the ^1H NMR spectra were collected at room temperature on a Bruker 800-MHz AVANCE III HD–type instrument equipped with a cryoprobe.

The concentrations of ammonium products were first determined at the wavelength of 420 nm by UV–Vis spectrophotometry. A certain amount of sample solution was first diluted to 25 mL in the colorimetric tube, and then both the potassium sodium tartrate solution (0.5 mL, 500 g/L) and Nessler's reagent (0.75 mL) were used as chromogenic agents before final testing.

In the ^1H-NMR measurement, the standard ammonium solutions [$(^{15}NH_4)_2SO_4$ and $(^{14}NH_4)_2SO_4$] with different concentrations were first prepared with 0.02 M Na_2SO_4. Both $Na^{15}NO_3$ and $Na^{14}NO_3$ were used as the N sources in the electroreduction experiment to get the $^{15}NH_4^+$ and $^{14}NH_4^+$ products, respectively; the pH of the obtained solution was adjusted to weak acid by 4 M H_2SO_4. Secondly, 0.01 g maleic acid ($C_4H_4O_4$) was used as the internal standard and was added to 25 mL standard ammonium solution. Then, 50 μL of deuterium oxide (D_2O) was mixed with 0.45 mL of the above-mentioned solution and tested in the NMR instrument to get the calibration curve; the $^{14}NH_4^+$ and $^{15}NH_4^+$ signals were distinguished by the triplet and doublet peaks, respectively. The ammonium concentrations were determined by the area ratios of NH_4^+-N and maleic acid peaks.

Nitrate was gradually reduced to ammonia according to the following paths (46):

$$NO_3^{2-}(*) + H_2O + e^- \rightarrow NO_2^-(*) + 2OH^- \quad [2]$$

$$NO_2^- \cdot (*) + e^- + H_2O \rightarrow NO(*) + 2OH^- \quad [3]$$

$$NO(*) + 2e^- + 2H^+ \rightarrow N(*) + H_2O \quad [4]$$

$$N(*) + H(*) \rightarrow NH(*) \quad [5]$$

$$NH(*) + H(*) \rightarrow NH_2(*) \quad [6]$$

$$NH_2(*) + H(*) \rightarrow NH_3(*) \quad [7]$$

The NFE was calculated according to Faraday's law as follows:

$$NFE = (n \times F \times C_{NH_4^+} \times V)/Q \quad [8]$$

where F represents the Faraday constant, n represents the stoichiometric coefficient of NO_3^- to NH_4^+, V is the solution volume, Q is the total of electricity consumed, and t is the reaction time.

The Tafel curve was used to assess the overpotential needed for nitrate reduction; the equation is as follows:

$$\eta = a + b \cdot \log(j) \quad [9]$$

where η represents the potential and j is the current density.

LSV polarization curves of Co SACs in nitrate or nitrite solution were examined at different scan rates from 50 to 130 mV/s. CV tests were performed 1,000 times with the scan rate of 60 mV/s in the 0.1 to −1.5 V potential window. The electron transfer number (n) for nitrate reduction was determined using the LSV peak current according to the following equation:

$$I_p = -2.99 \times 10^5 (n_c\alpha_c)^{1/2} ACD^{1/2} n\nu^{1/2} \quad [10]$$

where I_p, A, C, and D represent the peak current, electrode surface area (2.25 cm^2), nitrate concentration, and diffusion coefficient (2.0×10^{-5} $cm^2 \cdot s^{-1}$), respectively.

The ECSA of different samples was deduced as follows: First, different scan rates (2.5, 5.0, 7.5, 10.0, and 12.5 $mV \cdot s^{-1}$) were selected in the CV measurements within the non-Faradic potential range of −0.45 to −0.65 V; then the electrochemical double-layer capacitance (C_{dl}) was calculated through the slope of line fitted by the capacitive current differences [$(J_A - J_B)/2$] against the scan rates. Finally, the ECSA was obtained by calculating the ratio of C_{dl} to C_s, and the general capacitance with ideal smooth was used as C_s in the same electrolyte. EIS of Co-CN and Co-CNP was performed at an Ivium-type electrochemical workstation in the 1,000-kHz to 0.01-Hz region with 3-mV amplitude.

Computational Methods. All spin-polarized DFT calculations were performed based on the first principles (52, 53) through the generalized gradient approximation with the Perdew–Burke–Ernzerhof (54) formulation. The ionic cores were described by the projected augmented wave potentials (55, 56), and a plane wave basis set was used to evaluate the valence electrons with a kinetic energy cutoff of 400 eV. Gaussian smearing with 0.05-eV width was used, allowing partial occupied Kohn−Sham orbitals. The vacuum spacing in the vertical direction of plane was 15 Å, and 3 × 3 × 1 Monkhorst–Pack k-point sampling was used for Brillouin zone integration. The little electronic energy change ($<10^{-6}$ eV) indicates the reaching of self-consistency, and the ideal optimized structure was achieved when the energy change was smaller than 0.05 $eV \cdot Å^{-1}$.

The free energy (G) of the basic reaction was calculated as follows:

$$G = E + ZPE - TS \quad [11]$$

where E is the total energy and ZPE and TS represent zero-point energy and entropic variations, respectively.

The total energy of the optimized adsorbate on substrate (E_{ad+sub}), adsorbate energy (E_{ad}), and clean substrate energy (E_{sub}) were all calculated, and the final adsorption energy (E_{ads}) was calculated as follows:

$$E_{ads} = E_{ad+sub} - E_{ad} - E_{sub} \quad [12]$$

Data Availability. All study data are included in the article and *SI Appendix*.

ACKNOWLEDGMENTS. We acknowledge the National Natural Science Foundation of China (Grants Nos. 52091543, 72140003, 41977162) and the Beijing Natural Science Foundation (Grant No. JQ21031) for financial support of this work. The ^1H-NMR experiment was carried out at the BioNMR facility, Tsinghua University Branch of the China National Centre for Protein Sciences (Beijing). We thank Dr. Ning Xu for assistance in NMR data collection.

1. Bulletin on China's ecological environment of 2020. Ministry of Ecology and Environment of People's Republic of China. https://www.mee.gov.cn/hjzl/sthjzk/. Accessed 26 May 2021.
2. Investigation report on the groundwater quality and pollution in China. Institute of Hydrogeology and Environmental Geology, Chinese Academy of Geological Sciences. http://en.cags.ac.cn/. Accessed 17 May 2016.
3. Y. Tong *et al.*, Improvement in municipal wastewater treatment alters lake nitrogen to phosphorus ratios in populated regions. *Proc. Natl. Acad. Sci. U.S.A.* **117**, 11566–11572 (2020).
4. Z.-Y. Wu *et al.*, Electrochemical ammonia synthesis via nitrate reduction on Fe single atom catalyst. *Nat. Commun.* **12**, 2870 (2021).
5. G.-F. Chen *et al.*, Electrochemical reduction of nitrate to ammonia via direct eight-electron transfer using a copper–molecular solid catalyst. *Nat. Energy* **5**, 605–613 (2020).
6. D. H. Kim *et al.*, Selective electrochemical reduction of nitric oxide to hydroxylamine by atomically dispersed iron catalyst. *Nat. Commun.* **12**, 1856 (2021).
7. L. Su *et al.*, Tailoring the assembly of iron nanoparticles in carbon microspheres toward high-performance electrocatalytic denitrification. *Nano Lett.* **19**, 5423–5430 (2019).
8. R. Jia *et al.*, Boosting selective nitrate electroreduction to ammonium by constructing oxygen vacancies in TiO_2. *ACS Catal.* **10**, 3533–3540 (2020).
9. J. Gao *et al.*, Non-precious Co_3O_4-TiO_2/Ti cathode based electrocatalytic nitrate reduction: Preparation, performance and mechanism. *Appl. Catal. B* **254**, 391–402 (2019).
10. C. Chen, K. Li, C. Li, T. Sun, J. Jia, Combination of Pd–Cu catalysis and electrolytic H_2 evolution for selective nitrate reduction using protonated polypyrrole as a cathode. *Environ. Sci. Technol.* **53**, 13868–13877 (2019).
11. J. M. McEnaney *et al.*, Electrolyte engineering for efficient electrochemical nitrate reduction to ammonia on a titanium electrode. *ACS Sustainable Chem. Eng.* **8**, 2672–2681 (2020).
12. J. Gao, B. Jiang, C. Ni, Y. Qi, X. Bi, Enhanced reduction of nitrate by noble metal-free electrocatalysis on P doped three-dimensional Co_3O_4 cathode: Mechanism exploration from both experimental and DFT studies. *Chem. Eng. J.* **382**, 123034 (2020).
13. J.-X. Liu, D. Richards, N. Singh, B. R. Goldsmith, Activity and selectivity trends in electrocatalytic nitrate reduction on transition metals. *ACS Catal.* **9**, 7052–7064 (2019).
14. S. Garcia-Segura, M. Lanzarini-Lopes, K. Hristovski, P. Westerhoff, Electrocatalytic reduction of nitrate: Fundamentals to full-scale water treatment applications. *Appl. Catal. B* **236**, 546–568 (2018).
15. E. L. Clark *et al.*, Influence of atomic surface structure on the activity of Ag for the electrochemical reduction of CO_2 to CO. *ACS Catal.* **9**, 4006–4014 (2019).
16. H. Zou, W. Rong, S. Wei, Y. Ji, L. Duan, Regulating kinetics and thermodynamics of electrochemical nitrogen reduction with metal single-atom catalysts in a pressurized electrolyser. *Proc. Natl. Acad. Sci. U.S.A.* **117**, 29462–29468 (2020).
17. L. Ma *et al.*, Emerging metal single atoms in electrocatalysts and batteries. *Adv. Funct. Mater.* **30**, 2003870 (2020).
18. S. Ji *et al.*, Chemical synthesis of single atomic site catalysts. *Chem. Rev.* **120**, 11900–11955 (2020).
19. H. Wang *et al.*, Doping monolayer graphene with single atom substitutions. *Nano Lett.* **12**, 141–144 (2012).
20. J. Wan *et al.*, In situ phosphatizing of triphenylphosphine encapsulated within metal–organic frameworks to design atomic Co_1–P_1N_3 interfacial structure for promoting catalytic performance. *J. Am. Chem. Soc.* **142**, 8431–8439 (2020).
21. C. Ren *et al.*, Relative efficacy of Co–X_4 embedded graphene (X=N, S, B, and P) electrocatalysts towards hydrogen evolution reaction: Is nitrogen really the best choice? *ChemCatChem* **12**, 536–543 (2020).
22. Y. Zhu *et al.*, Scale-up biomass pathway to cobalt single-site catalysts anchored on N-doped porous carbon nanobelt with ultrahigh surface area. *Adv. Funct. Mater.* **28**, 1802167 (2018).
23. T. Sun *et al.*, Single-atomic cobalt sites embedded in hierarchically ordered porous nitrogen-doped carbon as a superior bifunctional electrocatalyst. *Proc. Natl. Acad. Sci. U.S.A.* **115**, 12692–12697 (2018).
24. W. Liu *et al.*, Single-site active cobalt-based photocatalyst with a long carrier lifetime for spontaneous overall water splitting. *Angew. Chem. Int. Ed. Engl.* **56**, 9312–9317 (2017).
25. Q.-L. Zhu *et al.*, Atomically dispersed Fe/N-doped hierarchical carbon architectures derived from a metal–organic framework composite for extremely efficient electrocatalysis. *ACS Energy Lett.* **2**, 504–511 (2017).
26. Y. Li *et al.*, Atomically dispersed Fe-N-P-C complex electrocatalysts for superior oxygen reduction. *Appl. Catal. B* **249**, 306–315 (2019).
27. P. Chen *et al.*, Atomically dispersed iron–nitrogen species as electrocatalysts for bifunctional oxygen evolution and reduction reactions. *Angew. Chem. Int. Ed. Engl.* **56**, 610–614 (2017).
28. S. Yang *et al.*, Exfoliated graphitic carbon nitride nanosheets as efficient catalysts for hydrogen evolution under visible light. *Adv. Mater.* **25**, 2452–2456 (2013).
29. Y. Ha *et al.*, Atomically dispersed Co-pyridinic N-C for superior oxygen reduction reaction. *Adv. Energy Mater.* **10**, 2002592 (2020).
30. J. Zhang *et al.*, Tuning the coordination environment in single-atom catalysts to achieve highly efficient oxygen reduction reactions. *J. Am. Chem. Soc.* **141**, 20118–20126 (2019).
31. H. Demirkiran, Y. Hu, L. Zuin, N. Appathurai, P. B. Aswath, XANES analysis of calcium and sodium phosphates and silicates and hydroxyapatite–Bioglass45S5 co-sintered bioceramics. *Mater. Sci. Eng. C* **31**, 134–143 (2011).
32. Y. Li *et al.*, Electrochemical synthesis of phosphorus-doped graphene quantum dots for free radical scavenging. *Phys. Chem. Chem. Phys.* **19**, 11631–11638 (2017).
33. G. Socrates, *Infrared and Raman Characteristic Group Frequencies: Tables and Charts* (Wiley, Chichester, UK, ed. 3, 2001).
34. Y. He *et al.*, Single cobalt sites dispersed in hierarchically porous nanofiber networks for durable and high-power PGM-free cathodes in fuel cells. *Adv. Mater.* **32**, e2003577 (2020).
35. X. Yang *et al.*, Nitrogen-doped porous carbon: Highly efficient trifunctional electrocatalyst for oxygen reversible catalysis and nitrogen reduction reaction. *J. Mater. Chem. A* **6**, 7762–7769 (2018).
36. B. Ni *et al.*, Optimized enhancement effect of sulfur in Fe–N–S codoped carbon nanosheets for efficient oxygen reduction reaction. *ACS Appl. Mater. Interfaces* **12**, 23995–24006 (2020).
37. Y. Liu *et al.*, Highly enhanced visible-light photocatalytic hydrogen evolution on g-C_3N_4 decorated with VOPc through π-π interaction. *Chin. J. Catal.* **40**, 168–176 (2019).
38. Y. Chen *et al.*, Atomic-level modulation of electronic density at cobalt single-atom sites derives from metal–organic frameworks: Enhanced oxygen reduction performance. *Angew. Chem. Int. Ed. Engl.* **60**, 3212–3221 (2021).
39. P. Li, Z. Jin, Z. Fang, G. Yu, A single-site iron catalyst with preoccupied active centers that achieves selective ammonia electrosynthesis from nitrate. *Energy Environ. Sci.* **14**, 3522–3531 (2021).
40. H. Zhang *et al.*, Unveiling the activity origin of electrocatalytic oxygen evolution over isolated Ni atoms supported on a N-doped carbon matrix. *Adv. Mater.* **31**, e1904548 (2019).
41. Y. Yao, S. Zhu, H. Wang, H. Li, M. Shao, A spectroscopic study of electrochemical nitrogen and nitrate reduction on rhodium surfaces. *Angew. Chem. Int. Ed. Engl.* **59**, 10479–10483 (2020).
42. A. Verdaguer-Casadevall *et al.*, Probing the active surface sites for CO reduction on oxide-derived copper electrocatalysts. *J. Am. Chem. Soc.* **137**, 9808–9811 (2015).
43. G. E. Dima, G. L. Beltramo, M. T. M. Koper, Nitrate reduction on single-crystal platinum electrodes. *Electrochim. Acta* **50**, 4318–4326 (2005).
44. M. Duca, M. O. Cucarella, P. Rodriguez, M. T. M. Koper, Direct reduction of nitrite to N_2 on a Pt(100) electrode in alkaline media. *J. Am. Chem. Soc.* **132**, 18042–18044 (2010).
45. Y. Zhao, N. K. Rao, L. Lefferts, Adsorbed species on Pd catalyst during nitrite hydrogenation approaching complete conversion. *J. Catal.* **337**, 102–110 (2016).
46. A. Thornton, P. Pearce, S. A. Parsons, Ammonium removal from solution using ion exchange on to MesoLite, an equilibrium study. *J. Hazard. Mater.* **147**, 883–889 (2007).
47. O. Lahav, M. Green, Ammonia removal using ion exchange and biological regeneration. *Water Res.* **32**, 2019–2028 (1998).
48. G. Diana *et al.*, Simultaneous phosphate and ammonia removal from aqueous solution by a hydrated aluminium oxide modified natural zeolite. *Chem. Eng. J.* **271**, 204–213 (2015).
49. A. Farkas, M. Rozić, Z. Barbarić-Mikocević, Ammonium exchange in leakage waters of waste dumps using natural zeolite from the Krapina region, Croatia. *J. Hazard. Mater.* **117**, 25–33 (2005).
50. L. Ori *et al.*, Sustainable removal of ammonia from anaerobic-lagoon swine waste effluents using an electrochemically-regenerated ion exchange process. *Chem. Eng. J.* **218**, 214–222 (2013).
51. Y. Pan *et al.*, Regulating the coordination structure of single-atom Fe-N_xC_y catalytic sites for benzene oxidation. *Nat. Commun.* **10**, 4290 (2019).
52. G. Kresse, J. Furthmüller, Efficiency of ab-initio total energy calculations for metals and semiconductors using a plane-wave basis set. *Comput. Mater. Sci.* **6**, 15–50 (1996).
53. G. Kresse, J. Furthmüller, Efficient iterative schemes for *ab initio* total-energy calculations using a plane-wave basis set. *Phys. Rev. B Condens. Matter* **54**, 11169–11186 (1996).
54. J. P. Perdew, K. Burke, M. Ernzerhof, Generalized gradient approximation made simple. *Phys. Rev. Lett.* **77**, 3865–3868 (1996).
55. G. Kresse, D. Joubert, From ultrasoft pseudopotentials to the projector augmented-wave method. *Phys. Rev. B* **59**, 1758–1775 (1999).
56. P. E. Blöchl, Projector augmented-wave method. *Phys. Rev. B* **50**, 17953–17979 (1994).